Title

MR phase imaging with bipolar acquisition.

Journal

NMR in Biomedicine, 30(4)

Authors

Dagher, Joseph
Nael, Kambiz

Publication Date

2017-04-01

DOI

10.1002/nbm.3523

Peer reviewed

Published in final edited form as:

NMR Biomed. 2017 April ; 30(4): . doi:10.1002/nbm.3523.

MR Phase Imaging with Bipolar Acquisition

Joseph Dagher[*] and **Kambiz Nael**

Department of Medical Imaging, The University of Arizona, Tucson, AZ

Abstract

We have previously proposed a novel MR phase imaging framework (MAGPI) based on a 3-echo sequence that demonstrated substantial gains in phase SNR. We improve upon the performance of MAGPI by extending the formulation to handle (i) alternating gradient polarity (bipolar) readout scheme, and (ii) arbitrary number of echoes. We formulate the phase imaging problem using Maximum Likelihood (ML) estimation. The acquisition uses an optimized Multi-Echo Gradient Echo sequence. The tissue-phase estimation algorithm is a voxel-per-voxel approach which requires no reference scans, no phase unwrapping and no spatial denoising. Unlike other methods, our bipolar readout model is general and does not make simplifying assumptions about the even-odd echo phase errors. The results show that (a) our proposed bipolar MAGPI approach improves on the phase SNR gains achieved with monopolar MAGPI and (b) the phase SNR converges with the number of echoes more rapidly with bipolar MAGPI. Importantly, bipolar MAGPI enables phase imaging in severely SNR-constrained scenarios where monopolar MAGPI is unable to find solutions. The substantial phase SNR gains achieved with our framework are used here to (a) accelerate acquisitions (full brain 0.89mm in-plane resolution in 2min30sec) and (b) enable high-contrast high-resolution phase imaging (310μm in-plane resolution) at clinical field strengths.

Graphical Abstract

Bipolar (non-flyback) multi-echo readouts offer significant SNR advantages over monopolar echo readouts but introduce unknown phase errors. We present a novel MR phase imaging method which jointly disambiguates errors from bipolar readouts as well as errors from phase wrapping, phase noise and channel-dependent phase offsets. The approach, based on voxel-per-voxel Maximum-Likelihood Estimation, enables MR phase imaging in SNR-limited scenarios, such as at in-plane resolutions of 310μm at 3T.

[*] Corresponding author: jdagher@email.arizona.edu; 1609 N. Warren Bldg 211 Rm 110, Tucson, AZ, USA 85719; (520) 621-0809.

Keywords

MR Phase; Bipolar; Non-Fly-Back; Phase Offset; Coil Array; Eddy Current; Multi-Echo; Maximum Likelihood

INTRODUCTION

Numerous imaging methods require accurate quantitation from MR phase in order to extract important information about the underlying physiology (2, 3, 4, 5, 6, 7, 8). However, unlike the magnitude signal, there is paucity of work on the limits of phase Signal-to-Noise Ratio (SNR) and phase Contrast-to-Noise ratio (CNR) achievable with a given pulse sequence. Phase quantitation depends on overcoming the following fundamental limitations: short echo times suffer from low phase SNR due to small phase signal accumulation, mid-long echo times suffer from phase wrapping errors, and long echo times suffer (in addition to phase wrapping) from low SNR due to T2* magnitude signal decay (1, 5, 8, 10). We have proposed in (1) a framework (MAGPI) for optimal imaging of MRI phase that overcomes these trade-offs. The MAGPI framework designs the acquisition-processing chain jointly: an optimizer selects three echo times in a Multi-Echo GRE (MEGE) sequence such that a corresponding algorithm reconstructs the tissue-frequency, voxel-per-voxel, in a Maximum Likelihood (ML) fashion. The ML reconstruction step, together with the echo-time optimization step, guarantee the highest possible SNR of the estimated phase. MAGPI combines data from multiple receive coils, without a reference scan, and without the need for spatial processing and/or phase unwrapping. We have shown that MAGPI achieves substantial improvements in the phase estimate, resulting in phase SNR gains by up to an order of magnitude compared to existing methods (1).

One limitation of MAGPI as described in (1) is the monopolar readout pattern (aka, fly-back gradients) in the 3-echo MEGE sequence. This readout strategy forces echoes to be acquired with the same gradient polarity (11). Another strategy is to acquire echoes with alternating polarities (bipolar readout) thus allowing for a shorter inter-echo spacing, shorter acquisition times and higher SNR efficiency than monopolar acquisitions (12, 13, 14). The choice of

echo times with bipolar MEGE sequences would thus be less constrained than monopolar MEGE sequences (14).

However, bipolar readouts introduce an additional ambiguity in the phase domain due to unknown k-space misalignment (error) between even and odd echoes (12, 13, 15). These errors arise mainly from spatially-varying eddy currents and various timing imperfections in the hardware (13, 14, 16). The alignment errors are also present in monopolar readouts but are consistent across echoes, and therefore do not introduce artifacts in reconstruction.The processing and analysis of the bipolar phase data across echoes, already facing ambiguities of phase wrapping, noise and channel-dependent phase offsets, is thus made even more challenging. Methods in the literature attempt to estimate this spatially varying even-odd echo error but: (a) require additional reference scans (13, 14, 15), (b) neglect alignment errors along phase encode directions (17) (c) make simplifying assumptions about spatial linearity (17), and/or (d) do not consider the dependence of the error on each receive coil in the array (14, 16).

In this paper we extend the MAGPI framework in (1) to allow for bipolar readouts, without requiring a reference scan or making any assumptions about the even-odd echo error. Also, as a second contribution, we extend the MAGPI framework to operate on an arbitrary number of echoes, $N_T \geq 3$. We answer here the resulting two questions using theoretical predictions, numerical simulations and *in vivo* data:

($\mathcal{Q}1$) How does the ML estimate of tissue frequency change with the number of echoes?

($\mathcal{Q}2$) How does the ML estimate from bipolar MAGPI compare to that from our previously validated monopolar MAGPI (1)?

Discussions related to each of these questions will be preceded in the text by $\mathcal{Q}1$ and $\mathcal{Q}2$, respectively.

METHODS

Theoretical Considerations

Measurement Model and Problem Definition—We can show that the numerically-computed angle of a GRE measurement $m_{k,c}$ at echo time TE_k and channel element c is given by (1),

$$\Psi_{k,c}(x,y) \triangleq \angle \mathbf{m_{k,c}} = \phi_{\phi,c}(x,y) + \phi_{\mathbf{e/o},c}(x,y) + 2\pi\Delta B(x,y)\,TE_k + \mathbf{\Omega}_{k,c}(x,y) + 2\pi \mathbf{r}_{k,c}(x,y)\,, \quad [1]$$

where $2\pi\Delta B(x, y)TE_k$ is the underlying "tissue phase" and $\phi_{\phi,c}(x, y)$ is the spatially-varying channel-dependent phase offset of channel c. The tissue frequency term $\Delta B(x, y)$ accounts for both global and local deviations in the main magnetic field at location (x, y). $\phi_{e/o,c}(x, y)$ denotes the phase error of either the even ($\phi_{e,c}(x, y)$) or odd ($\phi_{o,c}(x, y)$) echoes in every

channel c. Previous methods in the literature have assumed that $\phi_{e/o,c}(x, y)$ either (a) varies linearly across the read-out direction, (b) does not vary along the phase-encode direction, and/or (c) is independent of channels c. The authors in (14) have shown that assumptions (a) and (b) in particular are not accurate. In this paper, we employ a general model that allows for arbitrary phase errors, for every receiver channel. The term $\Omega_{k,c}(x, y)$ in [1] is the phase contribution of the complex additive Gaussian noise term in echo TE_k and channel c. The integer $r_{k,c}(x, y)$ is a phase-wrapping term which forces the sum in [1] to be in the range $[-\pi, \pi)$. Hereafter, we drop the pixel subscripts (x, y) with the understanding that the remaining analysis applies separately to each voxel in the image.

The problem is to generate an estimate of ΔB from the angle measurements $\Psi_{k,c}$. The challenges associated with this task are: (i) unknown $\phi_{e/o,c}$, (ii) unknown $\phi_{\phi,c}$ and, (iii) the inherent trade-off between phase noise and phase-wrapping errors.

Proposed Solution - bipolar MAGPI—We have previously proposed in (1) a solution to the problem above for monopolar readouts. We adapt the MAGPI approach (1) here for the case where $\phi_{e/o,c}$ is nonzero and $N_T > 3$. We refer to the new method here as "bipolar MAGPI" to distinguish it from the "monopolar MAGPI" proposed in (1).

Pass I. *Find the most likely* Δ B that explains the angle buildup between echoes of same polarity: In the first pass, measurements from all channels $c = 1, 2, \ldots, N_c$ and echoes $k = 1, 2, \ldots, N_T$ are separated into two groups, the even echo group and the odd echo group. We pose the following ML estimation problem, independently for every voxel in the image: what is the most likely ΔB that explains the accumulated angle between echoes of the same polarity? Formally, we find $\Delta B = \widehat{\Delta B}_I$ that maximizes the dual-echo system-likelihood (1):

$$\mathscr{L}_I(\Delta B) = \prod_{\substack{k1,k2=\{1,\ldots,N_T\} \\ (k1,k2)\in \mathscr{P}_{E/O}}} \prod_c \mathscr{L}_{k1,k2,c}(\Delta B), \qquad [2]$$

where the likelihood $\mathscr{L}_{k1:k2,c}(\Delta B)$ is computed only between echoes $k1$ and $k2$ of same polarity (even, $\mathscr{P}_E$ or odd, $\mathscr{P}_O$). Unless the echo times were carefully chosen, the solution to this maximization step is not guaranteed to be unbiased and could suffer from phase-wrapping and noise sub-optimality (1). Furthermore, the system-likelihoods in [2] inherently reference echoes of same polarity, in order to cancel both $\phi_{e/o,c}$ and $\phi_{\phi,c}$. Thus, $\widehat{\Delta B}_I$ in this pass suffers from phase noise amplification (1). We mitigate this shortcoming in Passes II and III.

Pass II. *Estimate* $\phi_{\phi,c} + \phi_{\phi,c} + \phi_{o,c}$ *and* ϕ_{e0}: Consider the term, $\phi_{k,c}^{rem} \triangleq \angle \mathbf{m}_{k,c} \quad e^{-i2\pi\widehat{\Delta B}_I TE_k}$. $\phi_{k,c}^{rem}$ represents the angle data in [1] that remains unexplained by the ML estimate $\widehat{\Delta B}_I$ and can be attributed to (a) channel offsets plus even-odd phase errors $\phi_{\phi,c} + \phi_{e/o,c}$ and (b) any estimation error in $\widehat{\Delta B}_I$ (1). We have shown in (1) that

applying a simple low pass filter operation on the term $\phi_{k,c}^{rem}$ would separate phase offset terms ($\phi_{\phi,c} + \phi_{e/o,c}$ in this case) from noise. This is only true if the errors in Pass I's estimate $\widehat{\Delta B}_I$ were unbiased. The low-pass filter would then recover a quantity proportional to $R_e(k, c) \propto \exp(i(\phi_{\phi,c} + \phi_{e,c}))$, for k even, and $R_o(k, c) \propto \exp(i(\phi_{\phi,c} + \phi_{o,c}))$, for k odd. Taking the sum over k, $R_e(c) = \sum_k R_e(k,c)$ and $R_o(c) = \sum_k R_o(k,c)$, then dividing $R_e(c)$ by $R_o(c)$ yields an estimate of the even-odd echo error for every channel, $exp(i\phi_{eo,c}) \triangleq exp(i(\phi_{e,c} - \phi_{o,c})) \propto R_e(c)/R_o(c)$.

Pass III. *Find the most likely* ΔB that explains the angle of all echoes and in all channels: We re-estimate the tissue phase, this time without needing to resort to echo referencing. To do this, we multiply the original data $m_{k,c}$ by either the conjugate of $R_e(c)$ (for k even) or the conjugate of $R_o(c)$ (for k odd). This substracts the estimate of the channels phase offset and the even-odd echo error from all complex measurements. We can then solve for the most likely $\Delta B = \widehat{\Delta B}_{III}$ which maximizes the overall system-likelihood (1):

$$\mathscr{L}_{III}(\Delta B) = \prod_{k=1}^{N_T} \prod_c \mathscr{L}_{k,c}(\Delta B). \quad [3]$$

The system-likelihood in [3] is guaranteed by the MAGPI optimizer (see below) to possess one global maximum corresponding to an efficient estimate of ΔB.

Optimal Selection of Echo Times with MAGPI—The goal of the optimizer is to select TEs that guarantee that (i) $\widehat{\Delta B}_I$ from Pass I is unbiased, and (ii) $\widehat{\Delta B}_{III}$ from Pass III is both unbiased as well as minimum variance. We adapt here the optimization method in (1):

$$\left[TE_1^{opt}, TE_2^{opt}, \ldots, TE_{N_T}^{opt}\right] = \underset{\left[TE_1, TE_2, \ldots, TE_{N_T}\right]}{arg\,min} \left[\mathscr{D}\left(\mathscr{L}_{III}(\Delta B), \delta(\Delta B - \Delta B_0)\right)\right]_{\Omega_k, r_k, \Delta B_0} \quad [4]$$

$$\text{such that,} \quad \left[\mathscr{D}\left(\mathscr{L}_I(\Delta B), \delta(\Delta B - \Delta B_0)\right)\right]_{\Omega_k, r_k, \Delta B_0} \leq \epsilon_I \quad [5]$$

$$\& \quad \left[TE_1, TE_2, \ldots, TE_{N_T}\right] \in \mathscr{C}_{TE}. \quad [6]$$

The objective function in [4] minimizes the distance $\mathscr{D}(\mathscr{L}_{III}, \delta)$ between the system likelihood of Pass III and the ideal likelihood function. The latter is intuitively a Dirac delta function centered at the correct frequency ΔB_0. The constraint in [5] guarantees that the errors from Pass I are kept below the phase-wrapping threshold, i.e. are unbiased. This also guarantees no error-propagation to Passes II and III (1). $\mathscr{C}_{TE}$ in [6] is the set of allowable echo times, which takes into account constraints such as the minimum echo time (TE_{min}), maximum echo time (TE_{max}) and, minimum echo spacing (ΔTE_{min}) achievable with the pulse sequence of choice. This MAGPI optimizer selects N_T echoes which achieve an optimal solution in a target "worst-case voxel" with a minimum SNR_0 = 26dB (SNR at TE = 0, this corresponds to an SNR of 7.3 at TE = 30ms), T2* of 20ms and a maximum off-resonance frequency of ΔB_{max} = 300Hz (the latter is determined based on the largest field deviation expected in anatomy of interest) (1). We note here that, for a monopolar readout, at least N_T = 3 echo times are needed to find a solution to [4]. For bipolar acquisitions, the minimum N_T is 4, where the extra echo is needed in our implementation in Pass I which divides echoes into two sets, even and odd, with a minimum of two echoes in each. Despite of this, we expect the bipolar MAGPI optimizer to be able to find solutions to [4] for more constrained pulse sequences than monopolar MAGPI. As we will show, the reasons behind this important difference are the constraints of the optimization [5] and [6].

Numerical Simulations

We tested the performance of our proposed phase imaging framework on a modified Shepp-Logan numerical phantom. The phantom model used a 128 × 128 tissue frequency ΔB map for the phase, and a mono-exponential decay for the corresponding magnitude with T2*= 30ms. We simulated GRE acquisitions of this complex-domain object using an array of 16-channel receive coils (23) which takes into account channel-dependent phase offsets. We introduced phase errors between even echoes and odd echoes ($\phi_{eo,c}$) in bipolar acquisitions only. $\phi_{eo,c}$ was assumed to vary spatially in a quadratic fashion.

in Vivo MRI Acquisitions

The brain of healthy volunteers was imaged after approval was obtained from our Institutional Review Board (IRB) and informed consent was given by the subjects. All scans were done on a Siemens Skyra 3T with a 32-channel head coil. We collected data in four different types of GRE scans: a standard-resolution scan (Scan SR), a high resolution scan (Scan HR), an accelerated standard-resolution scan (Scan AC), and a very high resolution scan (Scan vHR). The basic sequence parameters for these scans are summarized in Table 1. For each of these scan types, we collected data using single echo and multi-echo readouts. The acquisition time for single-echo scans was the same as the multi-echo MAGPI scans. One of the aims of the in vivo experiments is to demonstrate the advantages of bipolar MAGPI over monopolar MAGPI in the unconstrained (Scan SR, TR= 50ms), somewhat constrained (Scan HR) and the more constrained (Scans vHR & AC) acquisitions.

For the multi-echo acquisitions, we conducted the following experiments:

1. For Scan SR, we collected data in the same subject at N_T = 3, 4 and 6 echoes using monopolar readouts, and N_T = 4, 6 and 7 echoes with bipolar readouts, both at an "unconstrained" TR of 50ms.
2. For Scan HR we acquired N_T = 3 and 4 echoes with monopolar readouts, and N_T = 4, 6 and 7 echoes for bipolar readouts, with TR = 37ms.
3. For Scan AC, we collected data in a third subject using bipolar readouts with N_T = 5 echoes. In order to accelerate acquisition, the TR in this scan was constrained to 27ms, and parallel acquisition was employed with an acceleration factor (iPAT) of 5. This allowed us to acquire a full brain scan in 2 min 25 sec.
4. For Scan vHR, we collected a bipolar readout scan (N_T = 7) in a subject at a particularly high in-plane spatial resolution of 310 × 310μm^2 (voxel volume 0.19mm^3).

We note that the N_T echoes used in the multi-echo readout experiments above were all designed by the MAGPI optimizer [4] according to the timing constraints of each of the scan types and readouts.

Phase Reconstructions

MAGPI method—For each voxel in the image we independently apply the monopolar MAGPI reconstruction algorithm, as detailed in (1). Similar prescription is followed for bipolar MAGPI with the modifications to Passes I-III outlined above.

Literature Methods—We have performed in (1) rigorous comparisons between 3-echo monopolar MAGPI and a collection of six different methods from the literature. We avoid repeating the same comparisons here and instead explore additional literature methods that could be utilized when $N_T > 3$.

i. Slope: This method computes the angle, from each channel and echo, then fits a line in a Least-Squares sense as a function of the acquired TEs (20). This simple approach has two limitations: (1) it does not take into account the even-odd echo phase error in bipolar acquisitions and, (2) it is limited by phase-wrapping errors between successive echoes.

ii. Average Division (Div): This popular method computes ΔB from the phase accumulated between a pair of echoes using phase conjugation with coherent summation across channels (21). For $N_T \geq 3$ we average the ΔB estimate obtained across pairs of successive echoes. Similar to the Slope method, this technique is limited by phase-wrapping errors for large echo steps. We only apply the above two techniques (Slope and Div) in numerical simulations where $\phi_{eo,c}$ and phase-wrapping ambiguities were intentionally suppressed and where the linear phase assumption is guaranteed to hold.

iii. Weighted Average Homodyne: This method is a multi-echo adaptation to a popular approach in Susceptibility Weighted Imaging (SWI). First, a "homodyne phase" image is generated at every echo according to the traditional process (22). Next, the resulting homodyne phase images are averaged across echo times. The weights in the averaging step

are chosen to favor long echoes but penalize echoes longer than T2* = 30ms, namely: a_t = TE $\exp(-^{\mathrm{TE}}/_{30\times10^{-3}})$, with $\sum_t a_t = 1$.

Performance Evaluation

Multi-Echo Advantage—In order to quantify how the quality of the ΔB estimate changes with the number of echoes (question $\mathcal{Q}1$), we define the Root Mean Squared Error (RMSE) gradient as:

$$\delta RMSE_{N_T} = 1 - \frac{RMSE(N_T)}{RMSE(N_T - 1)}, \quad [7]$$

where RMSE(N_T) is the RMSE of ΔB obtained with N_T echoes. Note that one desired property for a phase estimator is to generate ΔB maps whose RMSE(N_T) never increases with N_T (i.e., δRMSE$_{N_T} \geq 0$). The ideal phase estimator would converge to the minimum RMSE with the smallest number of echoes possible (i.e., δRMSE$_{N_T}$ rapidly converges to 0 as N_T increases).

Bipolar Readout Advantage—In order to compare the performances of monopolar and bipolar MAGPI (question $\mathcal{Q}2$), we compare the accuracy and precision of their respective ΔB estimates. We have shown in (1) that monopolar MAGPI yields unbiased estimates of ΔB. Thus if the resulting average difference between monopolar and bipolar MAGPI estimates is zero then this implies that the ΔB estimate from bipolar MAGPI is unbiased as well. In order to evaluate the precision advantage of bipolar readouts, we compare the RMSE of bipolar and monopolar MAGPI obtained at their respective maximum N_T, namely:

$$\gamma_{N_{T,max}} = \frac{RMSE\left(N_{T,max}^{mono}\right)}{RMSE\left(N_{T,max}^{bi}\right)} - 1. \quad [8]$$

The comparison is performed at $N_{T,max}$ where performance (RMSE) is expected to be the best (lowest). Information about convergence to this lowest RMSE is conveyed by δRMSE$_{N_T}$ in [7]. Finally, due to the more-lenient echo-timing constraints associated with bipolar readouts, we expect the RMSE reduction factor $\gamma_{N_{T,max}}$ to be always non-negative.

RESULTS

Numerical Simulations and Theoretical Predictions

We show in the first row of Figure 1 an example of the original numerical object. Rows 2-5 show typical reconstructed ΔB maps, at two values of SNR_0 (33dB and 27dB), obtained using the monopolar and bipolar MAGPI algorithms with Scan SR at TR = 50ms. Note that the maximum number of echoes that could fit in this TR for this sequence is 7 with monopolar readout and 9 with bipolar readout. This example shows that, as expected, the ΔB estimation performance improves with N_T for each of the monopolar and bipolar MAGPI algorithms. $\mathcal{Q}1$ Qualitatively, the ΔB estimate improves most visibly for both algorithms

after the first additional echo, i.e. between 3 to 4 echoes for monopolar MAGPI and 4 to 5 echoes for bipolar MAGPI. Quantitatively, the RMSE gradient δRMSE_{N_T} [7] for monopolar MAGPI was δRMSE_{N_T} = {22%, 11%, 10%, and 7%}, for N_T = {4, 5, 6, 7}, respectively, while for bipolar MAGPI δRMSE_{N_T} = {15%, 5%, 6%, and 6%}, for N_T = {5, 6, 7, 8}, respectively, for both SNRs. These measures correlate with the qualitative (visual) enhancement. $\mathcal{Q}2$ This example also shows that the bipolar MAGPI algorithm outper forms monopolar MAGPI, at all values of N_T and at both SNR_0, despite the fact that bipolar acquisitions have an added ambiguity term associated with ϕ_{eo} (Figure 1c). Ultimately, the RMSE reduction $\gamma_{N_{T,max}}$ [8] is 13% for SNR_0 = 33dB, and 11% for SNR_0 = 27dB. The final row in Figure 1 shows example reconstructions obtained with the Slope and Division methods, both using the same 7 echoes chosen by the monopolar MAGPI algorithm (rows 2 and 3, column 5). Given that no even-odd echo phase error (ϕ_{eo}=0) or phase wrapping ($2\pi\Delta B_{max}\text{TE}_{N_{T,max}} = 0.45\pi$rad) was introduced with these methods, any gain obtained with MAGPI (monopolar or bipolar) would thus only be due to improved noise-efficiency. Here, monopolar MAGPI outperforms both Slope and Division methods by a factor of 6.48 and 4.17, respectively, at SNR_0 = 33dB, and 6.24 and 7.87 respectively at SNR_0 = 27dB.

The results of Figure 1 correspond to a specific example numerical phantom. In order to compute the overall average RMSE for each method, SNR and N_T, one would need to create many random realizations of noise, ΔB, $\phi_{\text{eo},c}$ and $\phi_{\phi,c}$. Alternatively, we can approximate MAGPI's performance using the numerically-computed Minimum Variance Unbiased (MVU) bound associated with the designed System-Likelihood in [3] (1). We have performed extensive testing (not shown here) which assert that the MVU predictions are only 2% smaller than the average RMSE obtained from a Monte Carlo experiment. We plot in Figure 2a the predicted RMSE of ΔB as a function of N_T, for monopolar and bipolar MAGPI algorithms, for different values of SNR_0. Table 2 summarizes the RMSE gradients, δRMSE_{N_T}, and RMSE reduction factors, $\gamma_{N_{T,max}}$. The results confirm the trends observed in Figure 1. $\mathcal{Q}1$ First, as expected, the RMSE of ΔB decreases as either SNR_0 or N_T increases. Also, the RMSE improvement δRMSE_{N_T} decreases as N_T increases. Note that δRMSE_{N_T} does not vary with SNR as it is a relative measure of improvement in quality and would not depend on the initial signal budget. $\mathcal{Q}2$ The results in Figure 2a also show that bipolar MAGPI outperforms monopolar MAGPI by $\gamma_{N_{T,max}}$ = 12.5% for this standard resolution sequence. This gain does not depend on SNR_0.

We repeat the same RMSE computations as Figure 2a with more timing-constrained sequences. Specifically, we shorten the TR of Scan SR twice: first to 37ms in Figure 2b (TE_{max} = 34ms), and then to 32ms in Figure 2c (TE_{max} = 30ms). Finally, we compute in Figure 2d the RMSE associated with Scan HR (at TR= 37ms). $\mathcal{Q}2$ We note from Figure 2 that $N^{mono}_{T,max}$ rapidly gets smaller as the sequence timing constraints become more stringent (from Figure 2a to 2d). On the other hand, $N^{bi}_{T,max}$ does not change as drastically as $N^{mono}_{T,max}$.

We draw particular attention to Figures 2c and 2d where certain RMSE values for monopolar MAGPI are missing for low values of SNR_0 and small N_T. For example, in Figure 2c, the monopolar RMSEs for N_T = 3 for both SNR_0 = 26 and 27dB are omitted. $\mathcal{Q}2$ This absence of a solution represents the inability of the MAGPI optimizer [4] to find

monopolar echo times in $\mathscr{C}_{TE}$ [6] that guarantee an unbiased estimate in Pass I [5]. In other words, the timing constraints of a monopolar readout are too stringent for this value of SNR and N_T. For Scan HR, the set $\mathscr{C}_{TE}$ is so constrained for monopolar readouts that no unbiased solution is found at any value of N_T, for $SNR_0 < 28dB$. Solutions with bipolar readouts, however, were successfully obtained in Scan HR for SNR_0 as low as 26dB. We illustrate in Figure 3 the performance of monopolar and bipolar MAGPI in such low SNR and timing-constrained limits of Scan HR. As expected, $\mathscr{Q}2$ monopolar MAGPI estimates suffer from severe noise-induced phase-wrapping errors for SNRs lower than 28dB. On the other hand, bipolar MAGPI is able to achieve an efficient and robust estimate of ΔB, under the same SNR and echo-time constraints.

in Vivo

We present first the results associated with Scan SR and examine any bias differences between monopolar and bipolar MAGPI. Figures 4a and 4b show the resulting ΔB maps for $N_T = 4$ echoes. The difference between these images is shown in Figure 4c. Note that, while subtle, this frequency difference includes background variations and/or field drifts that occurred between the scans. In order to eliminate such global variations, we apply a high-pass filter directly on the ΔB images, resulting in Figure 4d (monopolar) and Figure 4e (bipolar) and their respective difference in Figure 4f. $\mathscr{Q}2$ The high-pass filtered images are practically identical with an average difference of 2×10^{-3}Hz. Hereafter, we mainly examine high-pass filtered ΔB maps (denoted by ΔB_{HPF}) in order to focus on noise properties of different estimates.

Similar to the numerical simulations and theoretical analysis above, we evaluate the performance of the ΔB estimate as a function of N_T for both, Scan SR with TR = 50ms (Figure 5) and Scan HR with TR = 37ms (Figure 6). For Scan SR, Figures 5a-c show ΔB_{HPF} images obtained with monopolar MAGPI for $N_T = 3$, 4 and 6, respectively, while Figures 5d-f show the results obtained with bipolar MAGPI for $N_T = 4$, 6 and 7, respectively. $\mathscr{Q}1$ Note that the qualitative performance of the ΔB_{HPF} maps from both methods improves with N_T, albeit less visibly at larger values of N_T. A similar set of results is shown for Scan HR in Figure 6. One notable difference with this scan is that the maximum N_T achievable with monopolar MAGPI is 4 for Scan HR, due to the increased ΔTE_{min} and reduced TR. $\mathscr{Q}1$ Note that the qualitative improvement with N_T is more visible in this scan than in Scan SR. $\mathscr{Q}2$ Also more visible with Scan HR is the improve ment in the quality of ΔB_{HPF} obtained with bipolar MAGPI as compared to monopolar MAGPI. We note the substantially improved quality obtained with any MAGPI method, irrespective of N_T, compared to single echo GRE (Figure 5g and Figure 6f).

We illustrate next the performance of bipolar MAGPI in two sequences with significant SNR and timing constraints [5] and [6]. The first is the sequence of Scan AC. The optimizer of bipolar MAGPI was able to fit 5 echoes in its short TR and guarantee a solution down to an SNR_0 of 26dB (expected with large acceleration factors). Figure 7 shows ΔB_{HPF} obtained using bipolar MAGPI with $N_T = 5$ (Figure 7a), and two reference methods: single-echo GRE at TE = 24ms (Figure 7b) and the Weighted Average method (Figure 7c). The SNR advantage with bipolar MAGPI can be easily seen here, with substantial reduction in noise

and improved CNR compared to the traditional single echo scan and Weighted Average method. Bipolar MAGPI's gain over Weighted Average despite using identical acquisition highlights the importance of pairing the MAGPI optimization process with the MAGPI reconstruction process. The second SNR-limited *in vivo* scan is Scan vHR. Unlike monopolar MAGPI, the optimizer for bipolar MAGPI was able to find optimal echoes for this sequence down to a low of SNR_0 = 26dB (expected with high resolution acquisitions). The result is shown in Figure 8. Columns 1-3 show ΔB_{HPF} obtained with bipolar MAGPI at N_T = 7 echoes, the traditional single echo GRE scan (TE = 30ms) and the Weighted Average method, respectively. The two rows correspond to different slices. A slice-combined homodyne image is shown in Figure 9 for the bipolar MAGPI estimates. This is obtained by averaging the individual ΔB_{HPF} images across a 3-slice slab (6mm), centered at the location of the slices in Figure 8.

DISCUSSION

We have previously proposed in (1) a framework for imaging the phase of the MR signal using an algorithm based on a 3-echo monopolar MEGE sequence. We improved here over the performance of the 3-echo monopolar MAGPI through two key technical developments. First, we extended MAGPI to operate on arbitrary number of echoes ($N_T \geq 3$). Second, we solved the problem of phase estimation with bipolar readouts. We used numerical simulations and MVU bound computations to carefully investigate the advantages of multi-echo bipolar readouts and the dependence of these gains on different GRE sequence parameters (Figure 2).

(Q1) How does the ΔB estimate improve with N_T?

The RMSE gradients δRMSE_{N_T} in Table 2 show that the majority of the RMSE improvement with MAGPI is attained with the first additional echo and that adding more echoes offers decreasing improvement in RMSE. Bipolar MAGPI maintains this overall trend across sequences with different SNR budgets and different timing constraints. The RMSE improvement with monopolar MAGPI, on the other hand, is severely limited by the constraints of the sequence. Eventually, the RMSE with bipolar MAGPI converges faster than monopolar MAGPI. For example, the initial improvement in RMSE ($\delta\text{RMSE}_{N_T=4}$) decreases with monopolar MAGPI as the sequence becomes additionally constrained (top to bottom row). The *in vivo* images in Figure 5 and Figure 6 are consistent with these observations. Specifically, the improvement in ΔB with monopolar MAGPI from 3 to 4 echoes is not as significant with Scan HR (more constrained) as it is with Scan SR (less constrained). This is predicted from our theoretical results in Table 2 where $\delta\text{RMSE}_{N_T=4}$ with monopolar MAGPI was predicted to be 19% for Scan SR (TR= 50ms) and 8.7% for Scan HR. We also note from Figures 5 and 6 that bipolar MAGPI improves most visibly with the inclusion of one additional echo ($\delta\text{RMSE}_{N_T=5}$) and the improvement is substantially reduced beyond 6 to 7 echoes, consistent with our numerical predictions.

We emphasize that MAGPI's RMSE never increases as more echoes are added ($\delta\text{RMSE}_{N_T} > 0$), for either monopolar or bipolar algorithms. This is due to the inherent ML-optimal weighting of data acquired at different echoes and receive coils (1). This important property

is not always true with other multi-echo methods, such as Division and Slope (Figure 1 bottom row). This explains the significant gains achieved with MAGPI's phase reconstruction, attaining RMSEs that are up to 7.5X smaller than the RMSEs of Slope or Division methods despite using the same echoes. These gains would be even higher in reality as phase wrapping ambiguities were purposefully suppressed with Slope and Division methods in simulations, for the sake of argument.

(Q2) Monopolar MAGPI vs Bipolar MAGPI?

We have shown in our simulations (Figure 1) and *in vivo* experiments (Figure 4) that, for an unconstrained SNR, monopolar and bipolar MAGPI achieve similar estimates of ΔB, with an average difference close to zero (less than 5×10^{-3}Hz), for all N_T and SNR_0. Since monopolar MAGPI is an unbiased estimator of ΔB (1), this also asserts the unbiased nature of bipolar MAGPI. We have also shown that, for the same accuracy, bipolar MAGPI improves over the precision of monopolar MAGPI. This can be seen from Table 2, third column, where we list the relative reduction in RMSE $\gamma_{N_{T,max}}$ obtained with bipolar MAGPI over monopolar MAGPI for different sequences. As the timing constraints on the monopolar readouts increase (top to bottom row), $\gamma_{N_{T,max}}$ increases from 12.5% to 27%. Our *in vivo* experiments from Scan SR in Figure 5 and Scan HR in Figure 6 support this observation: the phase SNR gain obtained with bipolar MAGPI over monopolar MAGPI is more pronounced for Scan HR ($\gamma_{N_{T,max}}$ = 27%) than Scan SR ($\gamma_{N_{T,max}}$ = 12.5%).

The more significant advantage of bipolar MAGPI is its ability to image MR phase in timing-limited and SNR-constrained scenarios where monopolar MAGPI is unable to guarantee optimality according to [4]. For example, we have shown in simulations (Figure 3) that, in a sequence with a long ΔTE_{min}, short TR and poor SNR, the ΔB estimate obtained with monopolar MAGPI suffered from noise-induced phase-wrapping artifacts. Bipolar MAGPI, however, achieved an efficient estimate with an order of magnitude gain in RMSE over monopolar MAGPI. We also show this behavior *in vivo* with Scan AC, where TR is particularly short and the SNR is low. There, monopolar MAGPI was only able to find N_T = 4 echoes which guarantee optimality for $SNR_0 \geq 31$dB. On the other hand, bipolar MAGPI found a solution to [4] with N_T = 5 echoes for $SNR_0 \geq 26$dB. The result is shown in the bottom row of Figure 7. The noise-induced phase-wrapping artifacts seen with monopolar MAGPI are consistent with our numerical predictions. This establishes the need to use bipolar MAGPI in such low SNR timing-constrained scenarios.

We used the SNR gains associated with bipolar MAGPI to image high-resolution phase at particularly small voxel volumes of $0.19mm^3$ with Scan vHR (Figure 8). The bipolar MAGPI result is a detailed ΔB_{HPF} image showing microstructures with high CNR, such as the deep medullary veins and cortical ribbon. The poor phase SNR normally present in such small voxel volumes is seen in the images obtained with the traditional single echo scan with the same acquisition time. The MAGPI-equivalent acquisition with a weighted averaging step in reconstruction recovers some of the phase SNR compared to single-echo GRE but is still largely inferior to the phase SNR and phase CNR obtained with bipolar MAGPI. The slice-combined phase images of Figure 9 show additional level of microstructure details

across a total of 3 slices centered around the slice of Figure 8. Note the particularly high SNR and CNR of the detailed microstructures.

Bipolar Phase Error

We comment here on the ability of bipolar MAGPI to generate an estimate of the receivers' even-odd phase error map $\phi_{eo,c}$ in Pass II. Proving the efficiency of the $\phi_{eo,c}$ estimate is beyond our goal here but, it is valuable to verify whether *in vivo* $\phi_{eo,c}$ maps fit our expectations. Figure 4g shows estimates of $\phi_{eo,c}$, in every channel, as obtained from Scan SR. We note the overall similarity of the $\phi_{eo,c}$ estimates across channels, although there are subtle differences expected from local Eddy current variations (12, 16). We add these $\phi_{eo,c}$ maps in complex domain $\left(\sum_c R_e(c)/R_o(c)\right)$ and obtain an estimate of ϕ_{eo}, shown in Figure 4h. A profile taken across the readout direction (horizontal direction) from Figure 4h is shown in Figure 4i. We note an expected dominant linear behavior, albeit a non-linear component is also present around pixel location 140. This is consistent with the results in (14) where the authors reported localized non-linearities that are relatively small and spatially slowly varying. As an additional sanity-test, we conducted the following experiment: we applied the same ϕ_{eo} estimation process of Pass II on multi-echo data acquired using a *monopolar readout.* That is, the bipolar MAGPI algorithm was applied on a monopolar multi-echo scan which should clearly possess no even-odd phase errors. The resulting ϕ_{eo} estimate and a profile through its center are shown in Figures 4j-k, respectively. As expected, the bipolar MAGPI algorithm reported ϕ_{eo} to be numerically close to zero (less than 0.009rad, or less than 0.04Hz at TE = 30ms). This strongly suggests that our ϕ_{eo} estimation procedure is consistent with expectations. Note that we have shown in (1) that MAGPI's three-pass algorithm results in negligible error propagation and that errors made in Pass II do not impact the accuracy (bias) of the estimate obtained from Pass III.

Limitations and Conclusions

A limitation of the presented method is the choice of the readout bandwidths with the MAGPI methods. In this work, we have fixed the bandwidth empirically in all MAGPI scans here to be 240Hz/pxl, i.e. large enough to accommodate 7 monopolar echoes with Scan SR. However, the optimal choice of the number of echoes (N_T) also depends on the echoes' bandwidths, and thus both should be jointly selected by the MAGPI optimizer. This is the subject of future development. All sequences in this work employed full flow-compensation for the first echo only. Depending on the application, the multi-echo GRE sequences could benefit from flow-compensation of additional echoes. This topic is beyond our scope here but has been addressed in the literature (24). Finally, we note that we have used high-pass filtering as one way to remove the background phase in the image and study the noise content of the resulting image ΔB_{HPF}. Other methods exist for improved background phase removal (25, 26) which balance noise regularization and accuracy. We opted to focus here on studying the noise content in unregularized images where the resolution of the phase estimate is not sacrificed.

In summary, we have proposed a new phase imaging method which takes advantage of the SNR gains associated with bipolar readouts. The method is based on voxel-per-voxel ML

phase estimation which is able to jointly disambiguate errors from phase wrapping, phase noise, channel-dependent phase offsets and even-odd echo phase errors, all in one consolidated acquisition and reconstruction routine. Our findings suggest that (1) bipolar MAGPI is superior to monopolar MAGPI proposed in (1), particularly in timing-constrained or SNR-starved scenarios and (2) the multi-echo advantage with bipolar MAGPI achieves its near-optimal performance with $N_T = 6$ echoes. We have shown that the substantial phase SNR gains achieved with our framework can be used to (a) accelerate acquisitions and (b) enable high contrast high resolution phase imaging at clinical field strengths.

ACKNOWLEDGMENTS

Research reported in this publication was supported by the National Institute Of Biomedical Imaging And Bioengineering of the National Institutes of Health under Award Number K25EB018355. The content is solely the responsibility of the authors and does not necessarily represent the official views of the National Institutes of Health.

The authors are grateful to Scott Squire for his help in data acquisition, and Eriko Yoshimaru, Ph.D., for the helpful discussions.

Abbreviations used

ML	Maximum Likelihood
SNR	Signal-to-Noise Ratio
CNR	Contrast-to-Noise Ratio
MAGPI	Maximum Ambiguity Distance for Phase Imaging
GRE	Gradient Echo
MEGE	Multi-Echo Gradient Echo
RMSE	Root Mean Squared Error
MVU	Minimum Variance Unbiased

REFERENCES

1. Dagher J, Nael K. MAGPI: A framework for maximum likelihood MR phase imaging using multiple receive coils. Magnetic Resonance in Medicine. 2015 DOI: 10.1002/mrm.25756.
2. Schweser F, Deistung A, Lehr BW, Reichenbach JR. Quantitative imaging of intrinsic magnetic tissue properties using MRI signal phase: An approach to in vivo brain iron metabolism? NeuroImage. 2011; 54:2789–2807. [PubMed: 21040794]
3. Schweser F, Sommer K, Deistung A, Reichenbach JR. Quantitative susceptibility mapping for investigating subtle susceptibility variations in the human brain. NeuroImage. 2012; 62:2083–100. [PubMed: 22659482]
4. Haacke, EM., Reichenbach, JR. Susceptibility weighted imaging in MRI: basic concepts and clinical applications.. In: Haacke, EM., Reichenbach, JR., editors. MRI: Basic Concepts and Clinical Applications. John Wiley & Sons; New Jersey: 2011.
5. Rieke V, Butts Pauly K. MR thermometry. Journal of Magnetic Resonance Imaging. 2008; 27:376–390. [PubMed: 18219673]

6. Lotz J, Meier C, Leppert A, Galanski M. Cardiovascular flow measurement with Phase-Contrast MR imaging: Basic facts and implementation. Radiographics. 2002; 22:651–671. [PubMed: 12006694]
7. Mariappan YK, Rossman PJ, Glaser KJ, Manduca A, Ehman RL. Magnetic resonance elastography with a phased-array acoustic driver system. Magnetic Resonance in Medicine. 2009; 61:678–85. [PubMed: 19132758]
8. Dagher J, Reese T, Bilgin A. High–resolution, large dynamic range field map estimation. Magnetic Resonance in Medicine. 2014; 71:105–17. [PubMed: 23401245]
9. Funai A, Fessler J, Yeo D, Noll D. Regularized field map estimation in MRI. IEEE Transactions on Medical Imaging. 2008; 27:1484–1494. [PubMed: 18815100]
10. Robinson S, Schödl H, Trattnig S. A method for unwrapping highly wrapped multi-echo phase images at very high field: UMPIRE. Magnetic Resonance In Medicine. 2014; 72:80–92. [PubMed: 23901001]
11. Cunningham C, Vigneron D, Chen A, Xu D, Nelson S, Hurd R, et al. Design of flyback echo-planar readout gradients for magnetic resonance spectroscopic imaging. Magnetic Resonance In Medicine. 2005; 54:1286–9. [PubMed: 16187273]
12. Buonocore MH, Gao L. Ghost artifact reduction for echo planar imaging using image phase correction. Magnetic Resonance In Medicine. 1997; 38:89–100. [PubMed: 9211384]
13. Chen, Nk, Wyrwicz, AM. Removal of EPI Nyquist ghost artifacts with two-dimensional phase correction. Magnetic Resonance In Medicine. 2004; 51:1247–1253. [PubMed: 15170846]
14. Yu H, Shimakawa A, McKenzie CA, Lu W, Reeder SB, Hinks RS, et al. Phase and amplitude correction for multi-echo water-fat separation with bipolar acquisitions. Journal of magnetic resonance imaging: JMRI. 2010; 31:1264–1271. [PubMed: 20432366]
15. Hennel F. Two-dimensional deghosting for EPI. Magnetic Resonance Materials in Physics. Biology and Medicine. 1999; 9:134–137.
16. Alecci M, Jezzard P. Characterization and reduction of gradient-induced eddy currents in the RF shield of a TEM resonator. Magnetic Resonance In Medicine. 2002; 48:404–407. [PubMed: 12210952]
17. Lu W, Yu H, Shimakawa A, Alley M, Reeder SB, Hargreaves BA. Water–fat separation with bipolar multiecho sequences. Magnetic Resonance in Medicine. 2008; 60:198–209. [PubMed: 18581362]
18. Dagher J. A Joint Acquisition-Estimation Framework for MR Phase Imaging. Proceedings of Information Processing in Medical Imaging, Isle of Skye, Scotland, Lecture Notes on Computer Science. 2015:9123.
19. Kay, S. Fundamentals of Statistical Signal Processing: Estimation Theory. Prentice Hall; 1993.
20. Chen N, Wyrwicz A. Correction for EPI distortions using multi-echo gradient-echo imaging. Magnetic Resonance In Medicine. 1999; 41:1206–1213. [PubMed: 10371453]
21. Robinson S, Grabner G, Witoszynskyj S, Trattnig S. Combining phase images from multi-channel RF coils using 3D phase offset maps derived from a dual-echo scan. Magnetic Resonance In Medicine. 2011; 65:1638–1648. [PubMed: 21254207]
22. Haacke EM, Xu Y, Cheng YCN, Reichenbach JR. Susceptibility weighted imaging (SWI). Magnetic Resonance In Medicine. 2004; 52:612–618. [PubMed: 15334582]
23. Guerquin-Kern M, Lejeune L, Pruessmann KP, Unser M. Realistic Analytical Phantoms for Parallel Magnetic Resonance Imaging. IEEE Transactions on Medical Imaging. 2012; 31:626–636. [PubMed: 22049364]
24. Xu B, Liu T, Spincemaille P, Prince M, Wang Y. Flow compensated quantitative susceptibility mapping for venous oxygenation imaging. Magnetic Resonance In Medicine. 2013; 72:438–445. [PubMed: 24006187]
25. Liu T, Khalidov I, de Rochefort L, Spincemaille P, Liu J, TsiourisJ, Wang Y. A novel background field removal method for MRI using projection onto dipole fields (PDF). NMR in Biomedicine. 2011; 24:1129–1136. [PubMed: 21387445]
26. Li W, Avram A, Wu B, Xiao X, Liu C. Integrated Laplacian-based phase unwrapping and background phase removal for quantitative susceptibility mapping. NMR in Biomedicine. 2013; 27:219–227. [PubMed: 24357120]

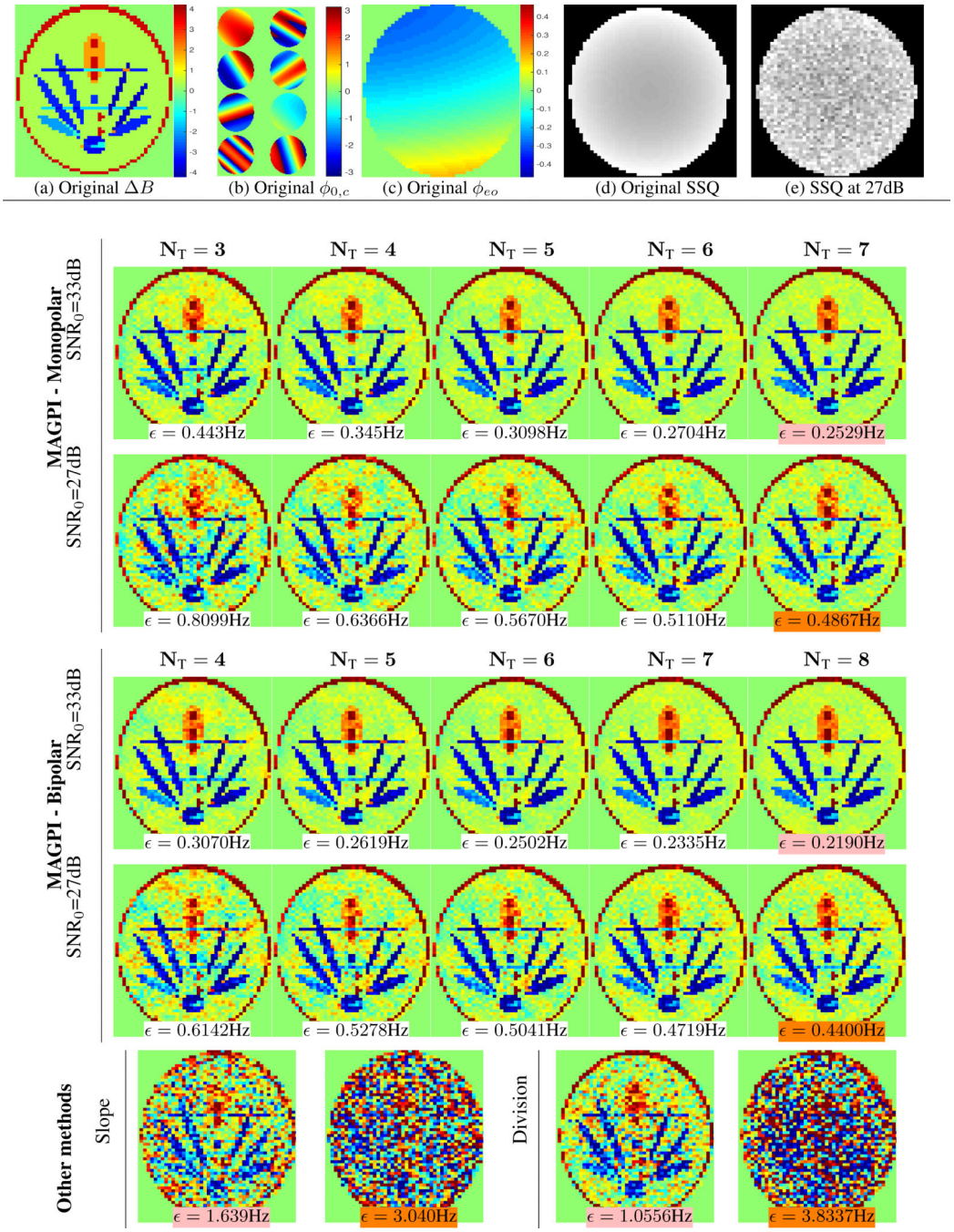

Figure 1.

(*previous page*) Numerical simulation results. First row shows an example phantom with (a) original tissue-frequency map ΔB, (b) channel-dependent phase offset map $\phi_{\phi,c}$, (c) even-odd phase error map ϕ_{eo} and, (d) original Sum of Squares (SSQ) image and (e) SSQ as measured at 27dB (or SNR= 8.23 at TE = 30ms). The second and third rows show example ΔB estimates as obtained using monopolar MAGPI, for SNR_0 of 33 and 27dB, respectively. The fourth and fifth rows show ΔB estimates obtained using bipolar MAGPI for the same SNR_0. The five columns correspond to different acquisitions with N_T = 3, 4, . . . , 7 echoes

for monopolar MAGPI and N_T = 4, 5, . . . , 8 echoes for bipolar MAGPI. The RMSE of each estimate is shown under the corresponding image, in Hz. Note that (1) ΔB estimate improves (RMSE decreases) as N_T increases for both monopolar and bipolar MAGPI and (2) bipolar MAGPI algorithm outperforms monopolar MAGPI at all values of N_T. The last row shows estimates obtained with the Slope method (columns 1 and 2), and the Division method (columns 3 and 4), with the image on left/right corresponding for SNR_0 = 33dB and 27dB, respectively. Both monopolar and bipolar MAGPI with N_T = 7 outperform the 7-echo Slope and Division methods by a factor of at least 6.5X and 4.2X, respectively, at SNR_0 = 33dB. The MAGPI gains are 6.3X and 7.87X at SNR_0 = 27dB. All ΔB maps share the same color-scale as Figure 1a.

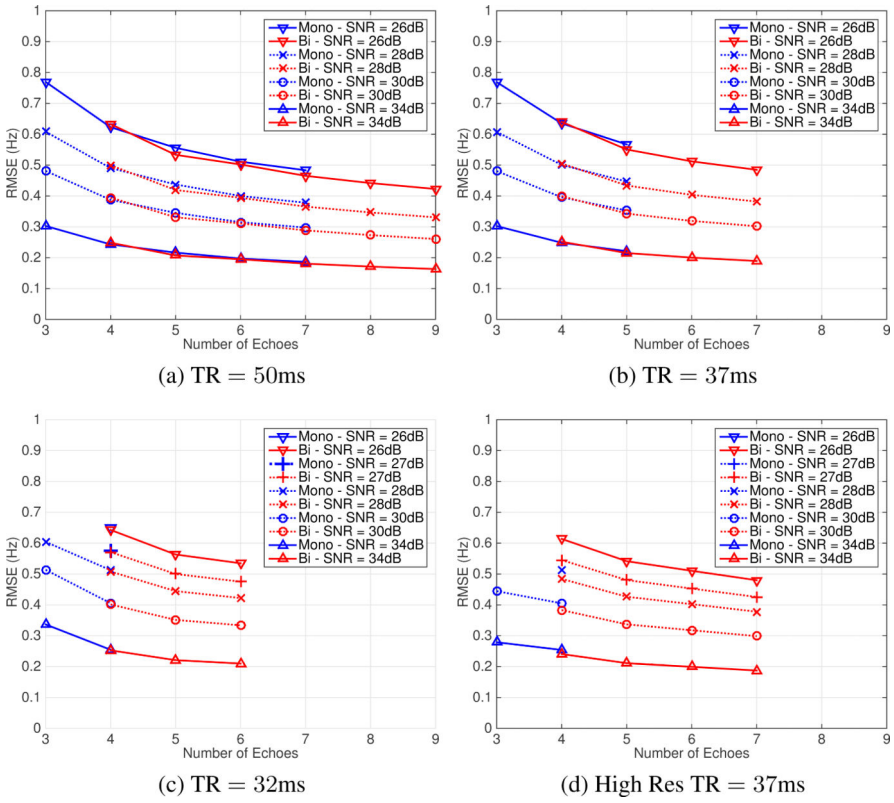

Figure 2.

The predicted RMSE plotted as a function of N_T (horizontal axis) for monopolar MAGPI (blue curves) and bipolar MAGPI (red curves), for different values of SNR_0 (line types). Figures 2a-2d correspond to the predicted performance of following sequences. (a) Scan SR with TR = 50ms, (b) Scan SR with TR = 37ms, (c) Scan SR with TR = 32ms and (d) Scan HR with TR = 37ms. The general observations are: (i) the improvement in the RMSE of MAGPI reduces as N_T increases and (ii) the RMSE reduction achieved with bipolar MAGPI over monopolar MAGPI increases as the sequence becomes more constrained, from Figure 2a (12% reduction) to Figure 2d (27% reduction).

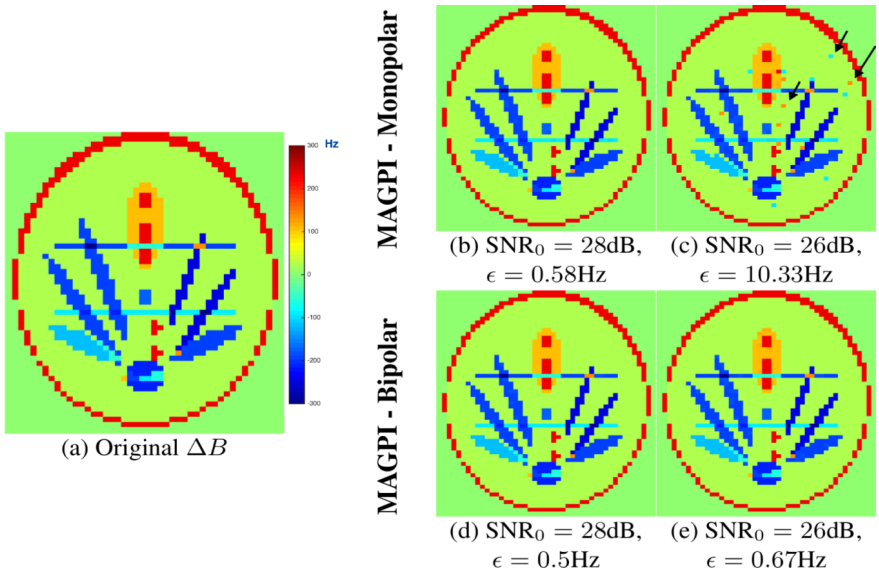

Figure 3.

MAGPI estimation performance simulated for Scan HR. (a) Original tissue-frequency map, note the dynamic range here is between [−300, 300]Hz. (b) and (c) are the monopolar MAGPI ΔB estimates at SNR_0 of 28 and 26dB, respectively. (d) and (e) show the corresponding bipolar MAGPI estimates at the same SNR_0. Similar to the results in Figure 1, monopolar MAGPI was able to achieve efficient estimation of ΔB for SNR_0 = 28dB, albeit with a slightly higher RMSE compared to bipolar MAGPI. However, monopolar MAGPI fails to find unbiased solutions for SNR_0 = 26dB, as seen with the noise-induced phase-wrapping artifacts in (c) (black arrows). This is explained by Figure 2d where monopolar MAGPI optimizer was unable to guarantee a solution to [4] for SNR_0 < 28dB. Bipolar MAGPI on the other hand achieves efficient and robust estimation at lower SNRs than monopolar MAGPI.

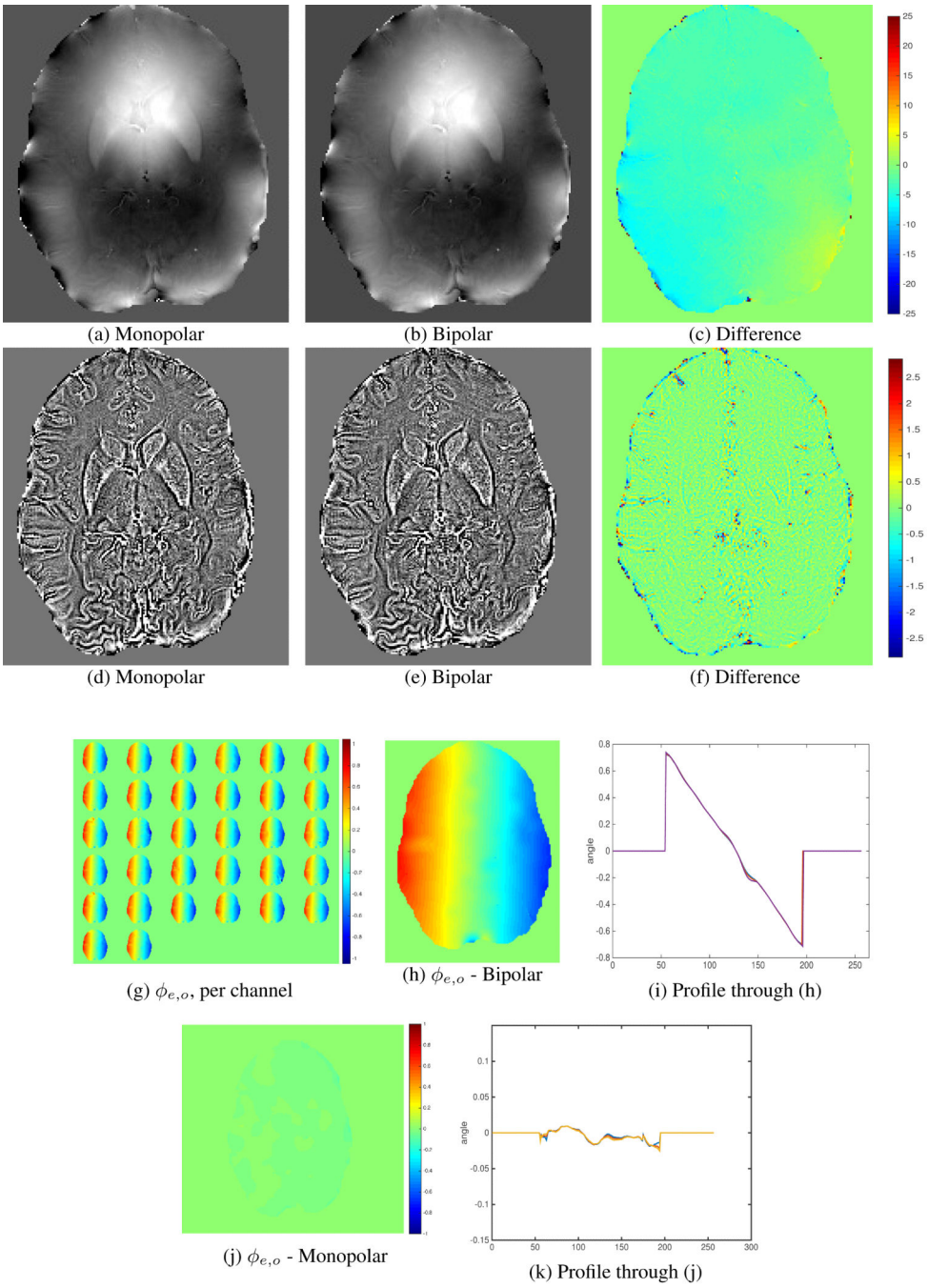

Figure 4.

(*previous page*) Results from the standard resolution *in vivo* Scan SR: ΔB estimate from (a) monopolar MAGPI and (b) bipolar MAGPI, both using $N_T = 4$ echoes. The difference between the 2 is shown in (c). The images in (a) and (b) are homodyne filtered and displayed in (d) and (e), respectively. The difference between the homodyne ΔB is shown in (f). The average difference in (f) is less than 2×10^{-3}Hz. The estimate of the bipolar even-odd echo error in every channel $\boldsymbol{\phi}_{\mathrm{eo},c}$ is shown in (g), which when combined over channels c according to Pass II yields $\boldsymbol{\phi}_{\mathrm{eo}}$ in (h). A profile taken across the center in the readout

(horizontal) direction of ϕ_{eo} is shown in (i). We observe a linear variation across readout direction, as normally assumed in the literature. However, we note the presence of a non-linear component around pixel locations 130-150. The final row (j and k) in this figure is a sanity test: our proposed bipolar MAGPI algorithm correctly estimates ϕ_{eo} to be numerically equal to zero in data that has been acquired in a monopolar fashion.

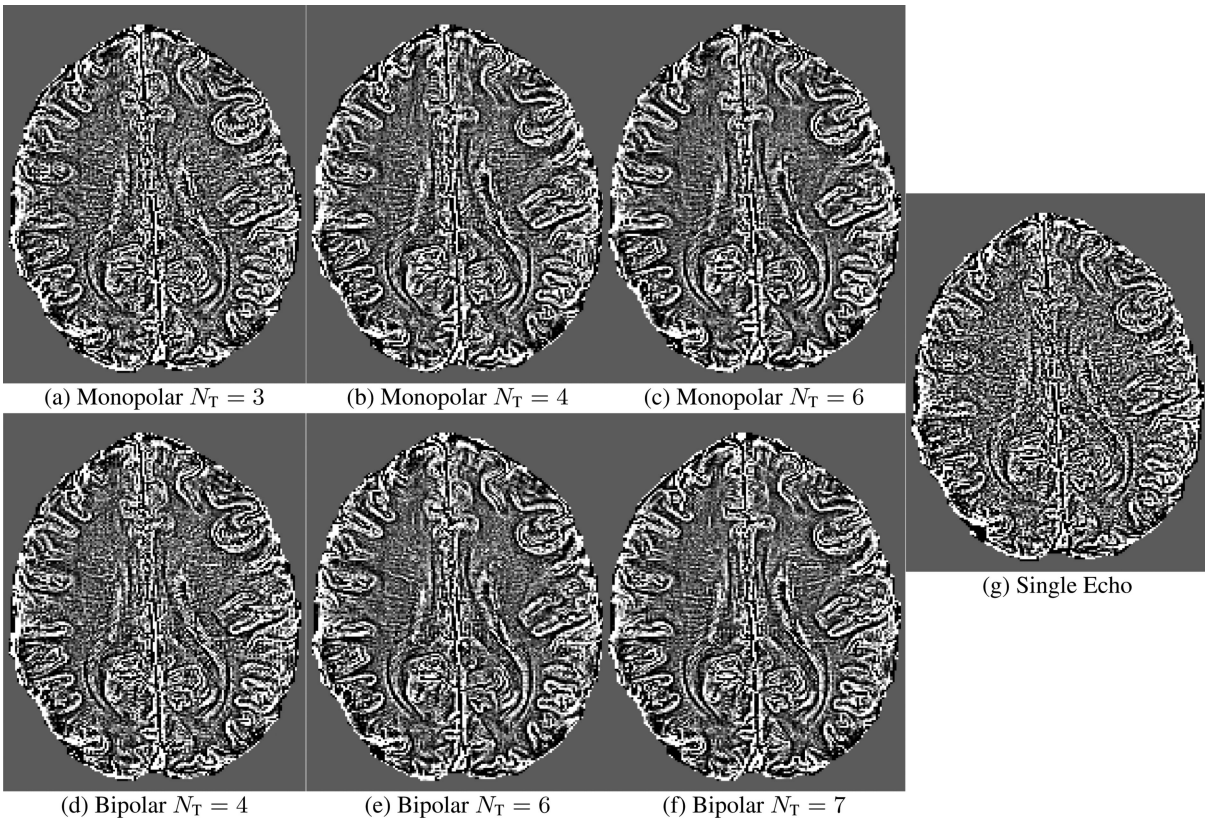

Figure 5.

Result from Scan SR with TR = 50ms. We compare the performance of monopolar MAGPI to bipolar MAGPI, across increasing N_T. The homodyne ΔB estimate obtained with monopolar MAGPI for (a) N_T = 3, (b) 4 and (c) 6 echoes. The equivalent result with bipolar MAGPI for (d) N_T = 4, (e) 6 and (f) 7 echoes. (g) Homodyne ΔB from the single echo GRE scan. We note a slight progressive improvement of image quality with increasing N_T (from left to right) for both monopolar and bipolar MAGPI. A slightly superior image quality using bipolar over monopolar MAGPI is more pronounced at the lowest N_T with better differentiation of white-gray matter and visualization of deep medullary veins. Both monopolar and bipolar MAGPI outperform the single echo GRE, as expected. All figures have been windowed between [−0.75,0.75] Hz.

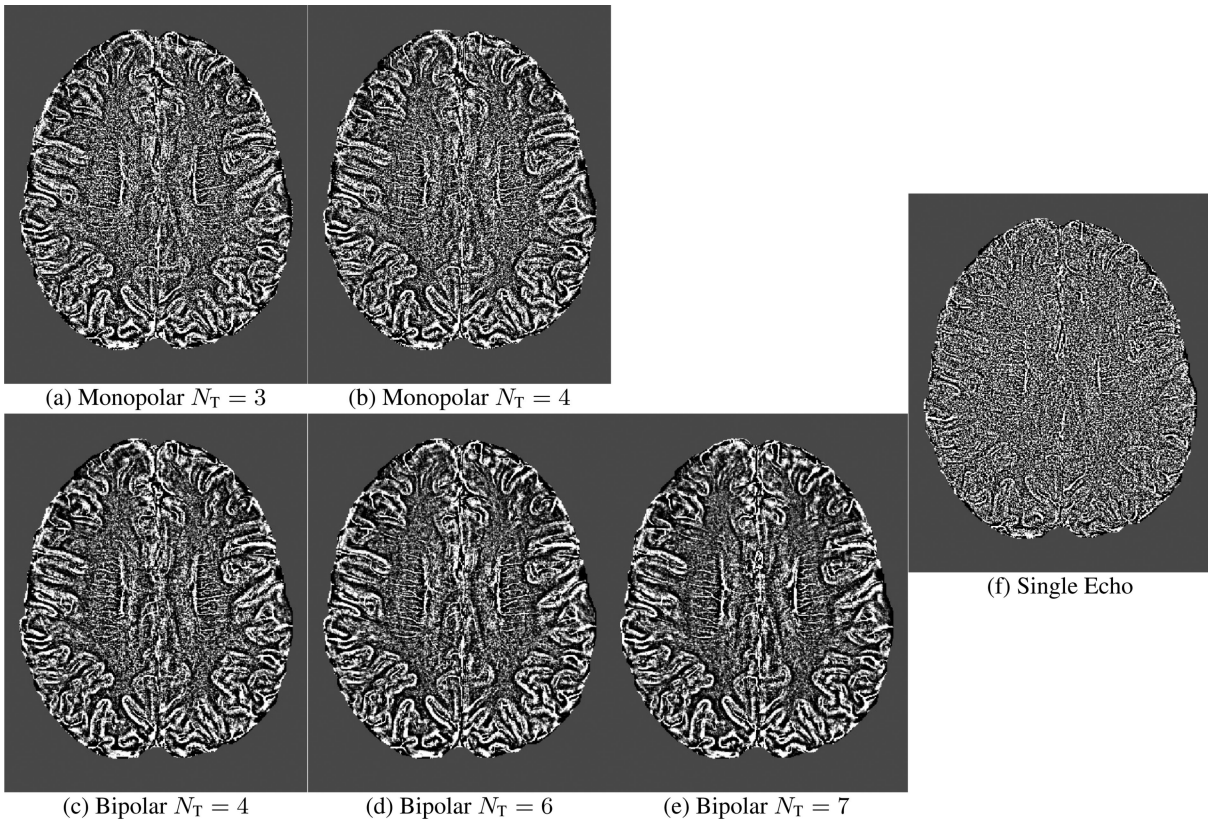

Figure 6.

Result from Scan HR with TR = 37ms. The setup of the figures here is similar to Figure 5. We note a clear performance gain with bipolar over monopolar MAGPI, with the superior CNR achieved in bipolar $N_T = 7$ over monopolar $N_T = 4$. Recall that, for this sequence, monopolar MAGPI is able to maximally fit 4 echoes. Also note significant improvement in conspicuity of cortical ribbon, white-gray mater differentiation and superior visualization of deep cortical and medullary veins. Bipolar MAGPI vastly outperforms the single echo GRE, as expected. All figures have been windowed between [−0.75,0.75] Hz.

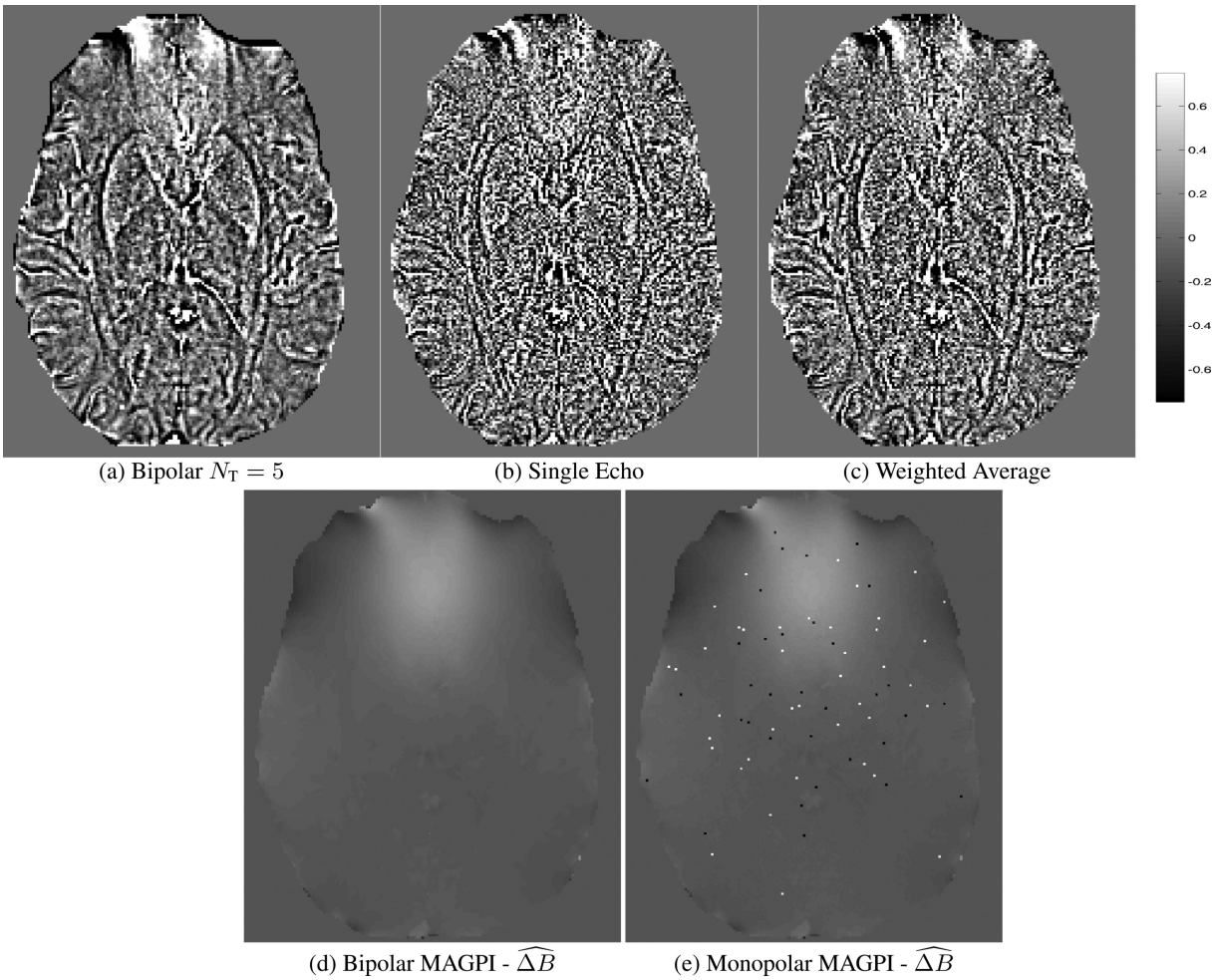

(a) Bipolar $N_T = 5$ (b) Single Echo (c) Weighted Average

(d) Bipolar MAGPI - $\widehat{\Delta B}$ (e) Monopolar MAGPI - $\widehat{\Delta B}$

Figure 7.

Result from Scan AC which acquires full brain data at a resolution of 0.89 × 0.89 × 2mm^3 in just under 2 minutes and 30 seconds. Homodyne ΔB as estimated using (a) bipolar MAGPI N_T = 5, (b) single echo GRE scan and (c) Weighted Averaging method. We note the fundamental reduction of the phase noise (gain in phase SNR and CNR) in the estimate of bipolar MAGPI, resulting in better depiction of basal ganglia and deep medullary veins. No spatial smoothing/averaging was ever employed with MAGPI. The bottom row compares the ΔB estimate obtained with (d) bipolar MAGPI to (e) monopolar MAGPI. Consistent with our numerical phantom predictions in Figure 3, we note the noise-induced phase-wrapping artifacts with monopolar MAGPI in such an SNR and timing-constrained scan.

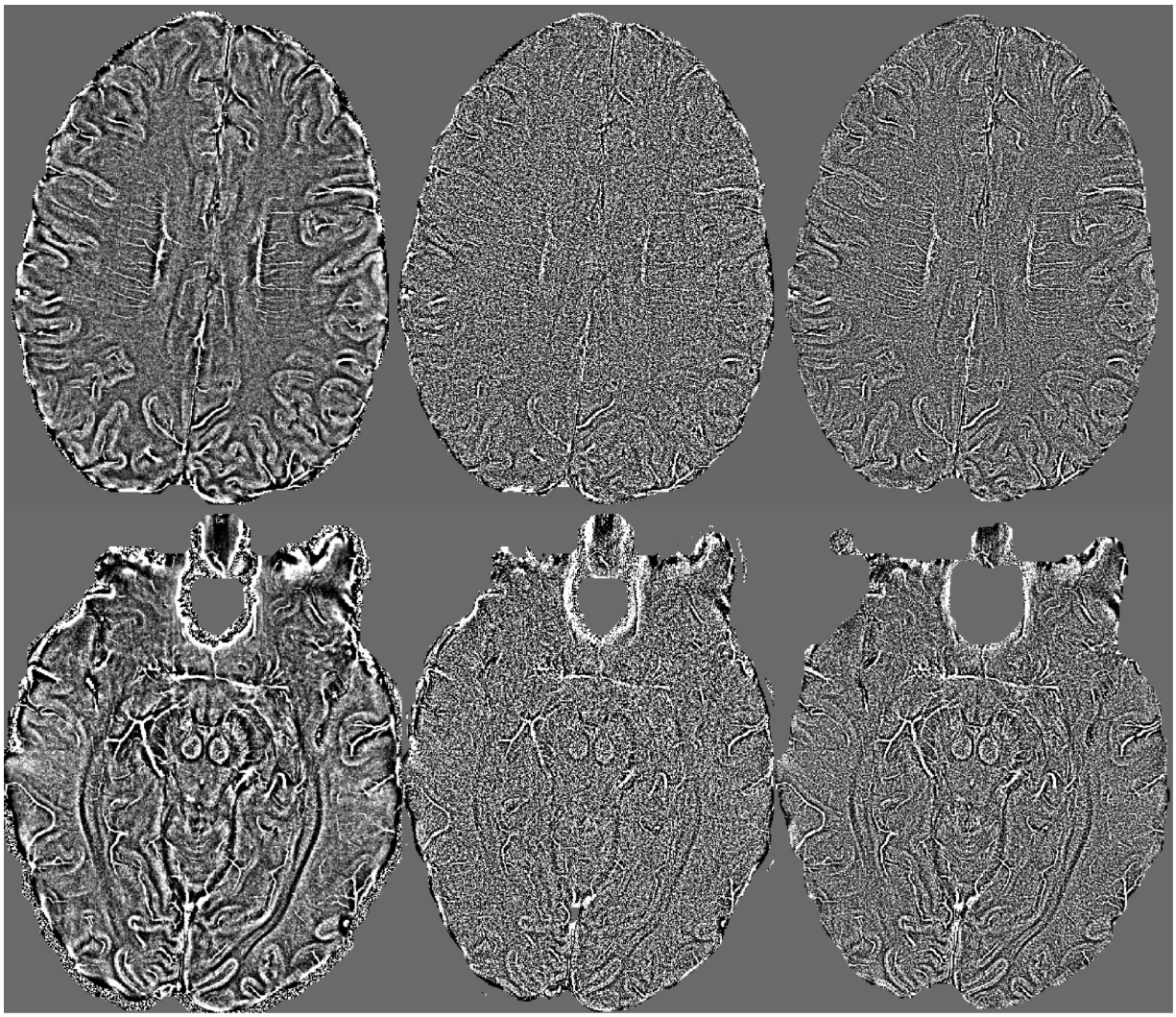

Figure 8.

Result from Scan vHR which acquires full brain data at a particularly high resolution of 0.31 × 0.31 × 2mm^3. The two rows correspond to two different slice locations. We display the homodyne ΔB as estimated using: (first column) bipolar MAGPI $N_T = 7$, (second column) single echo GRE and (third column) Weighted Average method which uses the same data as MAGPI. The acquisition time was the same for all sequences. We note the clear gain in phase SNR obtained with bipolar MAGPI, overcoming the spatial resolution limits traditionally achieved with phase imaging on a 3T. In the upper row, the single echo image has essentially non-diagnostic image quality. Note improved conspicuity of deep medullary veins and cortical ribbon in the Bipolar MAGPI image in comparison to Weighted Average image. In the lower row, note substantial improvement in diagnostic quality of the bipolar MAGPI resulting in accurate identification of deep brain structures such as substantia nigra and red nuclei. These structures are not well seen on single echo image and only seen with modest diagnostic quality in Weighted Average image. All figures have been windowed between [−0.75,0.75] Hz. No spatial smoothing/averaging was employed with MAGPI.

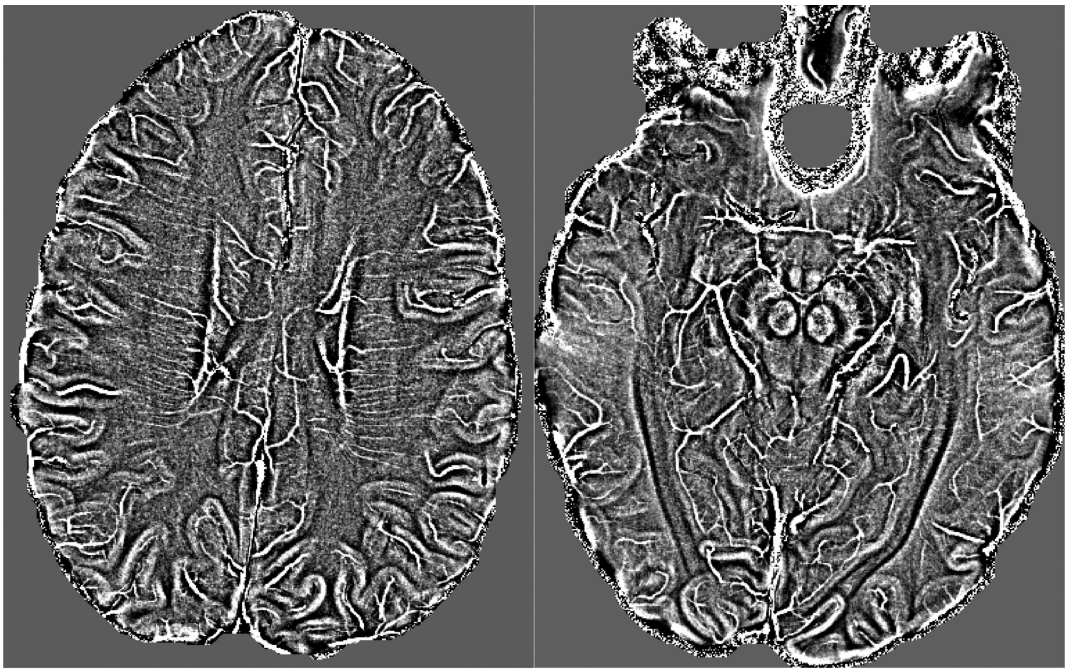

(a) Slice 19 (b) Slice 33

Figure 9.

A slice-combined homodyne ΔB for the bipolar MAGPI estimates from Figure 8. The effective slice thickness here is 6mm (3-slice average), with an in-plane resolution of 310μm. This estimate offers additional through-plane information displaying detailed brain microstructure at a high quality at 3T. Note the image quality of subcortical and deep medullary veins in (a) with near angiographic details. In (b), note significantly high image quality and details by which deep brain structures such as mammillary bodies, red nuclei, and substantia nigra are seen. All figures have been windowed between [−0.5,0.5] Hz.

Table 1

Sequences utilized in our numerical simulations, theoretical predictions and *In-Vivo* scans. iPAT is the acceleration factor used in parallel imaging.

Scan Type	**Parameters**	**Single-Echo**	**MAGPI - $\mathscr{C}_{TE}$**
Scan SR	3D GRE, N_x=256, N_y=232, N_z=50, FA=15°, Voxel: 0.86 × 0.86 × 2 mm^3, GRAPPA iPAT 2, TR=50ms.	BW=140Hz/pxl, TE = 30ms.	TE_{min}=6.1ms, TE_{max}=45ms, BW=240Hz/pxl, monopolar ΔTE_{min}=5.82ms, bipolar ΔTE_{min}=4.31ms.
Scan HR	3D GRE, N_x=512, N_y=464, N_z=50, FA=15°, Voxel: 0.43 × 0.43 × 2 mm^3, GRAPPA iPAT 2, TR=37ms.	BW=140Hz/pxl, TE = 30ms.	TE_{min}=8.18ms, TE_{max}=35ms, BW=240Hz/pxl, monopolar ΔTE_{min}=7.45ms, bipolar ΔTE_{min}=4.46ms.
Scan AC	Same as Scan SR, except: GRAPPA iPAT 5, TR=27ms, TA = 2min25s for full brain coverage.	BW=100Hz/pxl, TE = 24ms.	Same as Scan SR above except TE_{max}=26ms.
Scan vHR	3D GRE, N_x=608, N_y=546, N_z=50, FA=15°, Voxel: 0.31 × 0.31 × 2mm^3, GRAPPA iPAT 2, TR=45ms.	BW=140Hz/pxl, TE = 30ms.	TE_{min}=8.84ms, TE_{max}=35ms, BW=240Hz/pxl, monopolar ΔTE_{min}=8.02ms, bipolar ΔTE_{min}=4.48ms.

Table 2

The RMSE Gradient, or δRMSE_{N_T}, for both monopolar (column 1) and bipolar MAGPI (column 2) for different GRE sequences. For monopolar MAGPI, the first number in the sequence is the improvement obtained with to $N_T = 4$ as compared to $N_T = 3$ echoes, the second number is the improvement at $N_T = 5$ compared to $N_T = 4$, and so on. The same applies for bipolar MAGPI, except the first number is improvement at 5 echoes compared to 4. The last column lists the gain obtained with bipolar MAGPI over monopolar MAGPI at the maximum possible N_T in the sequence.

Scan Type	**δRMSE_{N_T} - Monopolar**	**δRMSE_{N_T} - Bipolar**	**$\gamma_{N_{T,max}}$**
Scan SR - TR = 50ms	{19%, 10.68%, 8.09%, 5.44%}	{16.54%, 6%, 7%, 5.31%, 4.6%}	12.5%
Scan SR - TR = 37ms	{17.77%, 10.84%}	{14.32%, 6.8%, 5.5%}	15%
Scan SR - TR = 32ms	{14%}	{12.55%, 4.97%}	19%
Scan HR - TR = 37ms	{8.7%}	{12.12%, 5.6%, 6%}	27%